Low-Cost Hold-Down and Release Mechanism for Small Satellite Deployable Solar Wings

Alexandre Florio
Space Flight Laboratory, University of Toronto Institute for Aerospace Studies
4925 Dufferin Street, Toronto, Ontario, Canada, M3H 5T6
aflorio@utias-sfl.net

Faculty Advisor: Dr. Robert E. Zee
Space Flight Laboratory, University of Toronto Institute for Aerospace Studies

ABSTRACT

Deployable structures increase mission capabilities and this applies particularly to microspace missions which are subjected to tight volume constraints. Nonetheless, these deployable structures come at an increase in risk and financial costs. In fact, problems associated to deployable solar wings are one of the main contributors to early mission failure. This paper presents the development of a reliable low-cost hold-down and release mechanism for a two-segment small satellite solar wing. This mechanism was valuable in the effort of bringing the overall solar wing cost down by 30% to 60% in comparison to what is commercially available. Its main components are the ejector release mechanism, the cups and cones, and the hold-down bracket. The ejector mechanism is a commercial off-the-shelf component with flight heritage. The cups and cones lock the panels together in-plane and support the in-plane loads. They were sized to support the launch loads while placing careful consideration on preventing them from impeding deployment. The bracket houses a spring-loaded bolt which is preloaded to keep the panels stowed. Its arched profile reduces shear forces on the inserts it mounts to, ultimately enabling a greater preload to be applied. Finite element analysis was performed to ensure positive strength margins. A thermal strain analysis verified that the coefficient of thermal expansion mismatch that is present within the mechanism does not damage the neighbouring solar cells. Thermal tests were executed and successfully verified that there were no risks associated to thermal strains on the cells and that the wing can fully deploy at operational temperature extremes. Finally, vibration tests were performed with the mechanism mounted to the satellite. The wing remained stowed for the entirety of the test with negligible shift in its stowed and deployed natural frequencies, proving that the components were sized properly. The wing was successfully deployed after the tests and inspections of the cups and cones showed minimal wear on the contact surfaces.

INTRODUCTION

Microspace missions have proven that valuable data can be acquired at lower cost and shorter lead times despite being constrained to relatively smaller volumes. To extend the capabilities of smaller satellites, deployable structures are essential. Nonetheless, they increase the complexity and thus increase the risk and cost of the mission.

Space Flight Laboratory (SFL) has extensive experience developing deployable structures from antennas to solar wings. It offers a variety of satellite platforms that can be tailored to the customer's payload needs. It has well-tested solutions for deployable solar wings for its SPARTAN bus, a nanosatellite, and for its DEFIANT bus, a microsatellite. This paper provides greater details on the development of the hold-down and release mechanism (HDRM) for the solar wings of the DAUNTLESS-EG (ESPA - Grande) bus, a small satellite. The latter weighs up to 500kg, supports payloads up to 300kg, and has overall dimensions of 1m x 1m x 1m. An HDRM is a system which safely keeps deployables stowed during launch and allows them to be released once in orbit.

According to a study from the Goddard Space Flight Center where 53 different spacecraft which suffered a deployable structure failure or anomaly between 1961 and 2017 were investigated, more than half of the deployment issues were related to deployable solar wings.[1] The problems were linked to tribology, mechanical loads, release mechanism issues, inadequate torque margin, and more. Furthermore, the School of Aerospace Engineering from Georgia Institute of Technology performed an analysis

of Earth-orbiting satellite reliability which included over 1,500 spacecraft from 1990 to 2008. They concluded that deployable solar wings are one of the main subsystems driving spacecraft failures in the first 30-days of operation, accounting for 17% of the failures.[2] A proper HDRM design is critical to ensure the reliability of deployable solar wings.

The microspace philosophy calls for low cost and versatile solutions that do not compromise on reliability by leveraging commercial off-the-shelf components (COTS), rapid prototyping, targeted tests, and small multi-disciplinary teams. Accordingly, the HDRM presented here is a simplistic and robust design which was a key factor in driving the overall solar wing cost down by 30% to 60% comparatively to what is commercially available.

DESIGN

The deployable solar wing for which the HDRM is designed is composed of two composite honeycomb panels which are stowed in a Z-fold and deploy by use of spring-loaded hinges (Figure 1). The wing weighs about 11.5kg and spans roughly 1.5m when fully deployed.
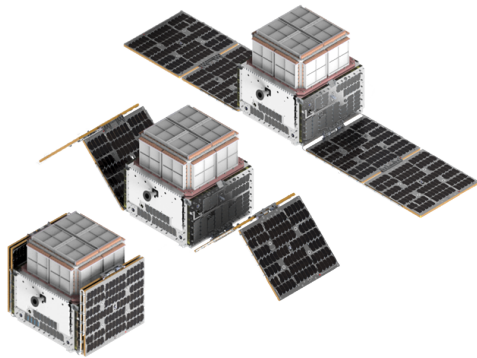

Figure 1: Wing Deployment

The main components which make up the HDRM are the ejector release mechanism (ERM), the cups and cones, the HDRM bolt, and the HDRM bracket (Figure 2).

The HDRM bracket is mounted and centered on the outer panel inner face using four blind inserts and supports the HDRM bolt. The HDRM bolt passes through both panels and screws into the coupler of the ERM (Figure 3). This bolt is carefully preloaded to ensure that the cups and cones do not separate under the launch loads.

The ERM allows the panels to be deployed when commanded by releasing the coupler. The type of

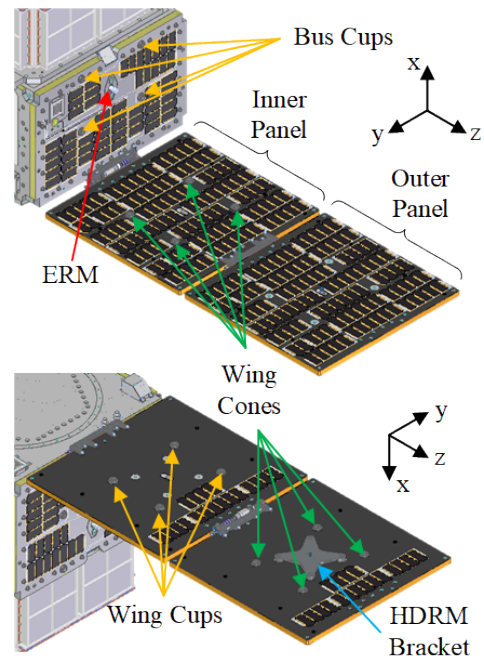ERM selected is a COTS component with flight heritage on previous SFL missions.

Figure 2: HDRM Components

For a nominal deployment path, the ERM coupler at the end of the HDRM bolt would not interfere with the ERM stem. That being said, in the event that the outer panel rotates significantly slower that the inner one, the coupler may interfere. If the latter happens while the satellite is in a cold state making the wing harness stiffer, the friction between the coupler and the stem may be too high for the spring-loaded hinges to be capable of fully deploying the wings. To mitigate this issue, a spring was integrated within the HDRM bracket to push off the HDRM bolt when it is released, clearing the stem before any significant rotation of the panels occurs (Figure 3).
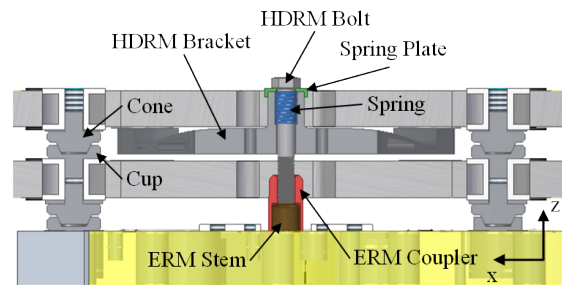

Figure 3: HDRM Section View

The spring plate is a U-channel piece which presses on the compression spring and is only locked

in rotation by holding on to the HDRM bracket square boss. It enables the HDRM bolt to be staked with epoxy to prevent it from loosening during launch. Otherwise, staking the bolt directly to the HDRM bracket would require a high enough ejection force to break the epoxy and allow the bolt to slide outward.

There are four cup and cone pairs between each pair of panels in a rectangular pattern centered with the ERM (Figure 2). They provide the main load path for the preload on the HDRM bolt. The ERM is designed to support axial loads only. Moreover, the hinges are not designed to resist the transverse loads as this would increase their size and complexity. Supporting the transverse loads is thus completed by the cups and cones. Here, the axial or out-of-plane loads act normal to the deployable solar wings in their stowed state (z direction), while the transverse or in-plane loads act parallel to the stowed wings (x and y directions). The cups and cones have a surface treatment increasing their surface hardness.

Requirements

The main requirements driving the design of the HDRM for the deployable solar wing are listed below (Table 1).

Table 1: Key Requirements

Number	Requirement	Validation Method
REQ1	The spacecraft bus (which includes the wings) shall meet the selected random vibration environments.	Analysis & Test
REQ2	The spacecraft bus (which includes the wings) shall apply the maximum axial static and lateral (transverse) quasi-static loads such that all worst-case combinations and directions of max tension, max compression, max shear, and max bending meet structural design requirements.	Analysis & Test

REQ3	The spacecraft bus (which includes the wings) shall be designed with Factors of Safety:
	
	• Metallic Structures:
	
	   – Ultimate Design Factor: 1.4
	   – Yield Design Factor 1.25
	
	• Composite/Bonded Structures:
	
	   – Ultimate Design Factor, discontinuity area: 2.0
	   – Ultimate Design Factor, uniform material: 1.5
		Inspection

Loads

To properly size the HDRM, the loads on the stowed wing need to be characterized. The main mechanical loads to analyze for are the quasi-static (QS) loads and the dynamic loads from random vibrations as per REQ1 and REQ2.

The wing is designed to be stiff enough such that its stowed first natural frequency is far apart from the satellite main vibration modes to minimize the dynamic amplification of the loads on the wing. The wing first natural frequency is about 1.45 to 2.35 times higher than the main satellite natural frequencies in the three orthogonal directions. As a result, the QS loads applied to the satellite were also applied to the wing for initial design and analysis purposes. Based on potential launch providers, the loads on a satellite of that size would be 10.8G. Following the European Cooperation for Space Standardization (ECSS) guidelines on structural analysis and multiplying the nominal launch loads by a factor of 2.25, the design accelerations on the wing and subsequently on the HDRM are 24.3G applied simultaneously in the axial, a_a, and transverse, a_t, directions (Figure 4). The multiplication factor was based on a qualification test factor accounting for the qualification loads, a project factor which accounts for the project maturity, a model factor which accounts for the mathematical uncertainties of the analysis, and a local design factor accounting for the complexity of the model.[3]

The dynamic loads from random vibrations were characterized from a finite element analysis (FEA) of the entire satellite. More precisely, the cups and cones were modeled as 1D elements and the root mean square (RMS) forces acting on them in all orthogonal directions were extracted. The vector sum of the 5-sigma loads on each cup and cone located between the wing and the satellite body panel represented the minimum load that the HDRM must support. In this case, transverse load is 6.8kN and the axial load is 3.9kN.

ANALYSIS

Cups and Cones

The cone geometry is driven by three main factors: HDRM preload, cup-cone jamming, and material strength.

The selection of the preload is of utmost importance. If improperly determined, the cups and cones will separate under the launch loads. Such separation will lead to a reduction in the wing stowed stiffness, significant wear on the cups and cones, and

considerable in-plane loads on the hinges and ERM. These may cause premature deployment or failure to deploy.

To determine the minimum preload required on the HDRM bolt, L_H, the forces on a single cone interfacing with a cup on the satellite bus are first investigated (Figure 4). The driving load case when analyzing for the quasi-static accelerations consists of a combined axial, A_a, and transverse acceleration loads, A_t, from the wing mass. L_P is the preload on a single cup. Due to symmetry, L_H can be assumed to be uniformly distributed amongst the 4 cup-cone interfaces.
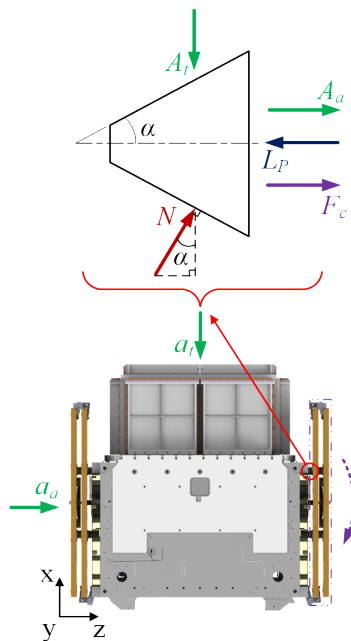
Figure 4: Cone Static Loads Diagram

The friction force is not included as this would limit the results of the analysis to certain materials for the cup and cones. Omitting it also provides a more conservative assumption to the minimum preload value and avoids reliance on friction to close the design which can be hard to predict. As a matter of fact, the coefficient of friction is affected not only by the material and surface roughness, but also by the frequency and amplitude of vibrations the parts are subjected to.[4]

With the center of gravity being offset from the shear plane of the cup-cone interface to the satellite, the acceleration will induce a couple on that interface as depicted by the purple dashed arrow in Figure 4. Two pairs of cups and cones will see an increase of the axial force equivalent to the magnitude of the force couple, F_c, while the opposite pairs will see a decrease of same magnitude.

The minimum L_P occurs at the onset of cup and cone separation. At that stage, the reaction or normal force, N, on the cone by the cup is only present to support A_t. Thus, from the summation of forces in the transverse direction, N can be calculated using (1) where α is the cup-cone half-angle. Note that d'Alembert's law is used below where the rate of change of momentum is treated as an inertial force.

$$\Sigma F_{\vec{t}} = 0$$
$$0 = N\cos\alpha - A_t$$
$$N = \frac{A_t}{\cos\alpha} \tag{1}$$

The minimum L_P is the minimum force to support A_a, F_c, and the axial component of N. It can be determined by (2) from the summation of forces in the axial direction. It will vary depending on the direction of the force couple.

$$\Sigma F_{\vec{a}} = 0$$
$$0 = A_a \pm F_c + N\sin\alpha - L_P$$
$$L_P = A_a \pm F_c + A_t\tan\alpha \tag{2}$$

Finally, the minimum L_H corresponds to the highest value of L_P calculated from (2) multiplied by the number of cup-cone interfaces as shown in (3). As L_H is equally distributed, using the highest value of L_P will ensure that all cup-cone pairs remain in contact.

$$L_H = 4 \cdot (A_a + F_c + A_t\tan\alpha) \tag{3}$$

Based on (3), the minimum L_H required to avoid cup-cone separation for the QS load case as a function of α is plotted in Figure 5.
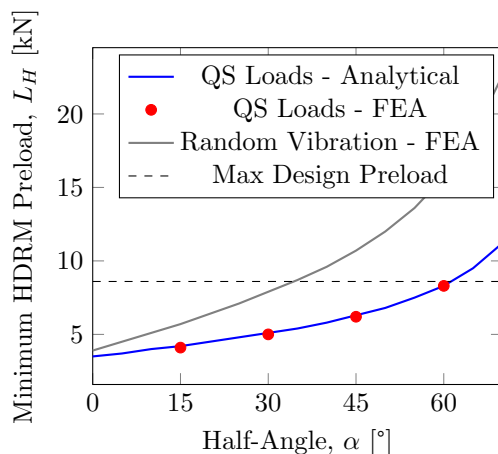

Figure 5: Minimum Preload to Maintain Cup-Cone Contact

To verify the analytical solution, a finite element model (FEM) was created where each cup and cone pair was modelled as a single 1D CGAP element. Such element allows a different stiffness to be set depending on whether it is under tension or compression. As such, by giving the element a zero-stiffness value when stretched and a high stiffness when compressed, the behaviour of the cup and cone contact in the axial direction was properly represented at a low computational cost. The minimum preload required against QS loads based on the FEA agreed with the analytical solution within $< 5\%$ (Figure 5).

As presented earlier, in the case of random vibration, the total loads on the cup-cone interfaces to the satellite were found to be 6.8kN in the transverse direction and 3.9kN in the axial direction. The minimum preload required was determined with the sum of the direct axial load and the axial component of the normal force that is present as a result of the transverse load (Figure 5). As observed in Figure 4, the latter force is dependent on α.

Due to uncertainties on multiple factors with the most influential one being friction, the preload on a torqued bolt can vary by $\pm\ 35\%$ when the bolt is non-lubricated.[5] This is commonly known as the preload scatter. The design or nominal preload must take into account this scatter. Knowing the maximum load that can be applied to the ERM by the manufacturer, the minimum HDRM preload that could occur on the HDRM as a result of aiming for that maximum preload is referred to as the maximum design preload in Figure 5. Thus, the minimum required preload must be lower than the maximum design preload for the design to be feasible. As observed in Figure 5, the random vibration environment is the limiting factor on the preload. To avoid separation at the cup and cone interfaces, α must be smaller than 33°.

To verify that the cup and cones do not seize along the deployment trajectory, two lines were plotted in a cross-sectional view taken perpendicular to the rotation axis: the location of the cup wall represented by a linear equation and the path of the cone tip represented by the equation of a circle (Figure 6). Both equations contained geometric parameters locating the cup-cone interface in space with respect to the hinge center of rotation. The equations were plotted for various α to determine if the path of the cone edge interferes with the location of the cup wall. Figure 7 shows the results for an α of 25° where nominal deployment is expected and for an α of 1° where the mechanism would seize. To avoid interference, the minimum α is 2°.
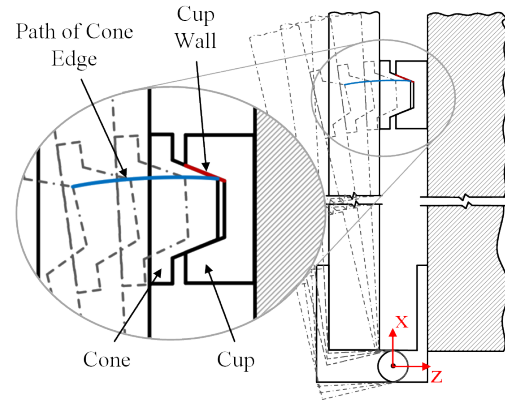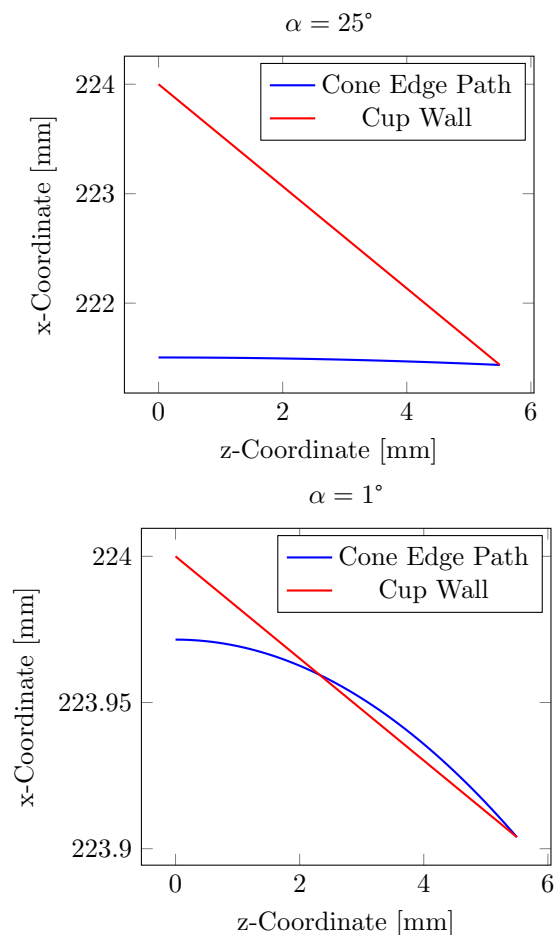

Figure 6: Cone Deployment Path

Figure 7: Deployment Path at Various Half-Angles

Another important verification on α is the interference fit between the cup and cone which could result in a self-holding taper joint. For such joint, the friction could seize the cups and cones together even after preload removal. This would lead to a

complete deployment failure. In this scenario, an interference fit is warranted to make the cup-cone joint stiffer and to properly support the transverse loads.

As presented in Figure 8, the axial components of the friction force, μN, and of N act in the same direction when the cone is preloaded. When the preload is released, N will still be present due to the interference fit. The axial component of the friction will now oppose N. Should the axial component of μN be greater than that of N, the cone will fail to separate from the cup. The minimum α to avoid a self-holding taper is determined by (4)[6] to be 22° based on a friction coefficient,[7] μ, of 0.4.

$$N \sin \alpha > \mu N \cos \alpha$$
$$\tan \alpha > \mu$$
$$\alpha > \tan^{-1} \mu \qquad (4)$$
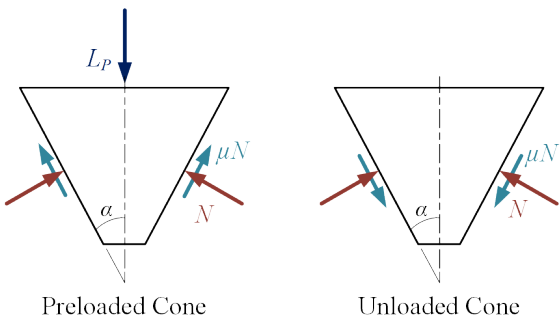
Figure 8: Self-Holding Taper Diagram

Based on the results from the cup-cone separation analysis, the deployment interference analysis, the self-holding taper analysis, and considering availability of standard machining tools, α was chosen to be 25° (or 50° full cone angle).

To determine the size of the cone, a FEM of a stand-alone stowed wing and supporting body panel was constructed (Figure 9). The objective was to determine the stress seen in the cups and cones as a result of the preload and launch loads. Due to contact analysis being computationally heavy, only the mesh of the cups and cones was refined. The rest of the components had a coarse mesh as only capturing their stiffness was relevant for this analysis, not their stress.

The bus body panel and the solar panels were modeled as 2D laminate elements with the facesheets and the core modeled independently. The cups, cones, hinge leaves, insert potting, and threaded inserts were modeled using 10-node, quadratic 3D solid elements. The mass of the miscellaneous hardware on the hinges such as the bearings and springs were modeled as lumped mass elements (0D) and connected to the hinge leaves using zero-stiffness RBE3 (Rigid Body Element) elements to avoid over-stiffening the hinges. RBE3 elements simply distributes the force from the source node to the target nodes based on a weighted average while RBE2 elements create connections of infinite stiffness. The solar cells on each face were modeled as non-inertial masses equally spread across the facesheet surfaces. The cups and cones connected to the threaded inserts with glue connections. The threaded inserts connected to the potting with glue connections and the potting connected to the panels in a similar way. Contact connections were used at the cup and cone interface. The HDRM screw was modeled as a 1D element. To help in the FEM setup and analysis, the mounting locations attaching the +Z panel to the spacecraft were connected to a central node via REB2 elements.
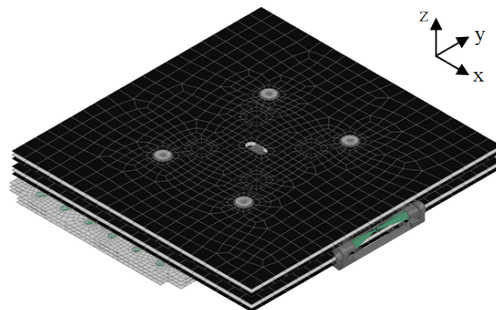

Figure 9: Cup-Cone Contact FEM

Due to manufacturing tolerances, the cups and cones will never see an exact fit. Thus, the tolerances were biased to always interface at the root of the cone as opposed to the tip to provide a greater surface contact area and greater stowed wing stiffness (Figure 10).
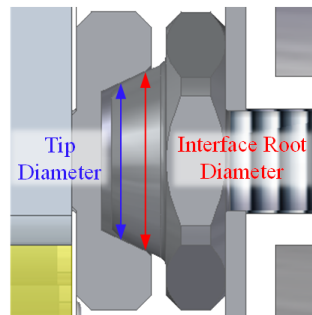

Figure 10: Root Diameter

The material strength margin, M_s, is calculated as per (5) where σ_m is the material strength, σ_c is the computed stress, and f is the factor of safety as per REQ3.

$$M_s = \frac{\sigma_m - f\sigma_c}{\sigma_m} \qquad (5)$$

The interface root diameter was varied to examine its impact on the stress margins. Sample results of the stress on the cups and cones are presented in Figure 11. It was observed that the regions of high stress were at the tip of the cone, the root of the cup, and the tip of the cup.
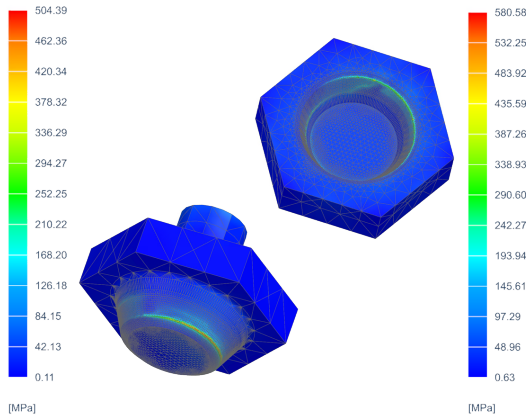

504.39
462.36
420.34
378.32
336.29
294.27
252.25
210.22
168.20
126.18
84.15
42.13
0.11
[MPa]

580.58
532.25
483.92
435.59
387.26
338.93
290.60
242.27
193.94
145.61
97.29
48.96
0.63
[MPa]

Figure 11: Contact Stress

Figure 12 shows that margins on the cone increase almost linearly within the interface root diameter range investigated. However, the cup margins seem to decrease past a certain diameter. Although the contact area increases as the root diameter increases, the cup wall thickness decreases. This explains why a stress increase is seen. The diameter leading to the highest critical M_s (26%) is 18.6mm.
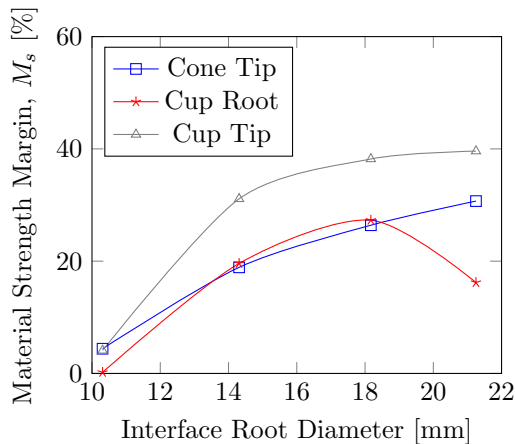

Figure 12: Contact Stress Margin

HDRM Bracket

The HDRM bracket supports the bolt which provides the preload to the stowed wing. The load

transfer between the HDRM bolt and the cups and cones goes through the 4 outer panel blind inserts on which the HDRM bracket mounts to. Assuming a typical preload scatter of $\pm\,35\%$ made the design difficult to close as the lower bound of the preload could be twice as small as the upper bound. On one hand, the preload must be high enough to prevent cup and cone separation, while on the other, it must be low enough to not damage the inserts. Consequently, multiple bolt, washer, helicoil insert, and lubrication combination were tested to characterize the joint. The combination which was ultimately selected had a scatter of $\pm\,15\%$ and a nominal preload was selected based on that scatter. The lower bound of the selected nominal preload respected the minimum preload as per Figure 5.

A FEM was constructed similar to Figure 9, but the cup-cone interface was modeled as a glue connection to reduce the computational cost and a finer mesh was used for most components, especially the HDRM Bracket. The bracket mounting screws were modeled as 1D elements. This allowed the extraction of the forces on the inserts and the computation of strength margins. The strength margin on the inserts, M_i, was computed based on (6) where P is the pull-out force, Q is the shear force, M is the moment, and T is the torsion on the insert.[8] The subscript ss refers to the permissible load.

$$M_i = \left(1 - \left[\left(\frac{P}{P_{ss}}\right)^2 + \left(\frac{Q}{Q_{ss}}\right)^2 + \left(\frac{M}{M_{ss}}\right)^2 + \left(\frac{T}{T_{ss}}\right)^2 \right] f^2 \right) \qquad (6)$$

As the HDRM bolt is preloaded, the bracket will tend to bow and bring the inserts towards the center as observed in Figure 13. This leads to high shear forces on the inserts.
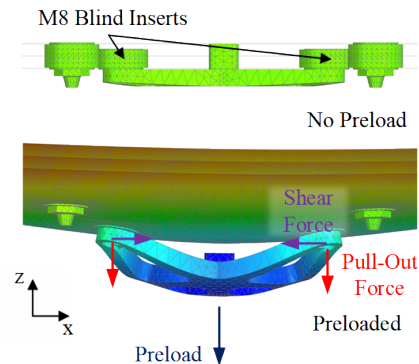

Figure 13: HDRM Bracket Shear

The original bracket design was not optimized to reduce the shear forces (Figure 14). In fact, the shear

force observed on each insert was equivalent to 2.2 times the pull-out force (Table 2). As a result, negative margins were seen on the insert strength. The insert strength was determined using ECSS standards and by coupon testing.

The next step was to see if a full plate could be stiff enough to reduce the shear forces. The results improved where the ratio of shear force to pull-out force decreased to 1.7, but the margins were still negative. Consequently, instead of only increasing the stiffness of the bracket, its profile was changed to cause some of the shear force to point outwards instead of inwards. To achieve this, the bracket was designed in the shape of an arch. Although the shear forces were still pointing inwards, this significantly reduced their magnitude and the ratio lowered to 1.0. This ultimately led to positive insert strength margins of 26%.
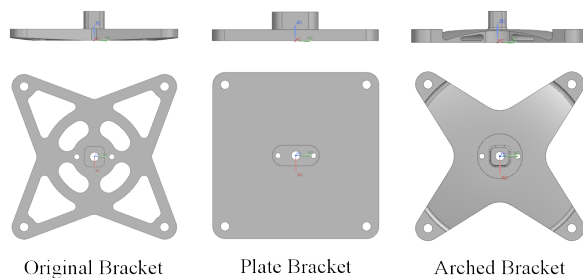

Original Bracket   Plate Bracket   Arched Bracket

Figure 14: HDRM Bracket Designs

Table 2: HDRM Bracket Characteristics

Bracket	Q/P Ratio	Mass [kg]	M_i [%]
Original	2.2	0.91	-69
Plate	1.7	2.06	-1
Arched	1.0	0.90	26

Inserts

For maximum strength of the blind inserts holding the HDRM bracket, they are fully potted. This also avoids the risk of creating an air gap even if the honeycomb core is perforated. A thermal strain analysis was performed to ensure that the deformations of the skin due to the potting won't damage the solar cells that rest on the opposite face of these inserts (Figure 15).

Titanium and aluminum inserts along with low, medium, and high coefficient of thermal expansion (CTE) potting material were analyzed. The material selection was performed to minimize the difference in CTE. A FEM of only the outer panel was created as the temperature extremes on the wing

would occur in that vicinity after deployment. The key elements of the FEM are shown in Figure 16.
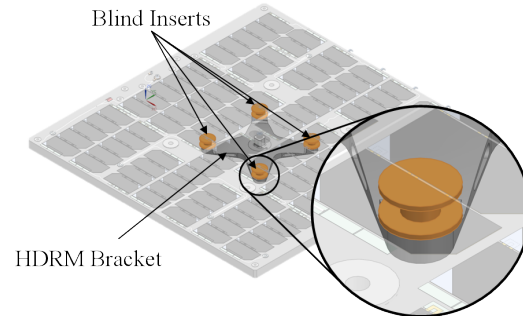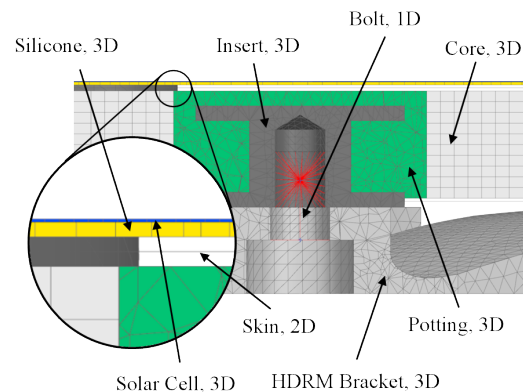

Figure 15: Solar Cells at Risk

Figure 16: Thermal Strain FEM

The FEM was subjected to delta hot and cold cases (Figure 17). The hot case delta varied from 20°C to 110°C while the cold case varied from 20°C to -100°C. The temperature extremes were based on expected non-operational limits of the deployed wing. The initial temperature corresponded to the approximate temperature at which the silicone would be applied (ambient temperature). The curvature of the solar cell at each node of the selected cross-sections was computed based on its displacement and that of the two pairs of nodes on either side of the node in question along the section line. More precisely, the curvature was found by obtaining the radius of a circle fitted to the five data points using the least squares method. The curvature margin, M_c, on the solar cells was determined using (7) where κ_a is the maximum curvature allowed given by the manufacturer and κ_c is the curvature measured from the FEM.

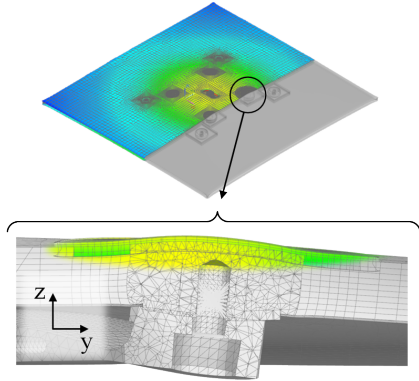$$M_c = \frac{\kappa_a - f\kappa_c}{\kappa_a} \tag{7}$$

Figure 17: Thermal Deformation (Cold Case)

The facesheets are made of carbon fiber which has a very low CTE. Due to being in direct contact with the core, the insert, and the potting which all have higher CTE's, the facesheets will shrink less at a cold temperature. This causes the bulge seen in Figure 18 on the solar cell. The dips on either sides of the bulge are a result of the core shrinking in one direction while the potting and insert shrinking in the other.
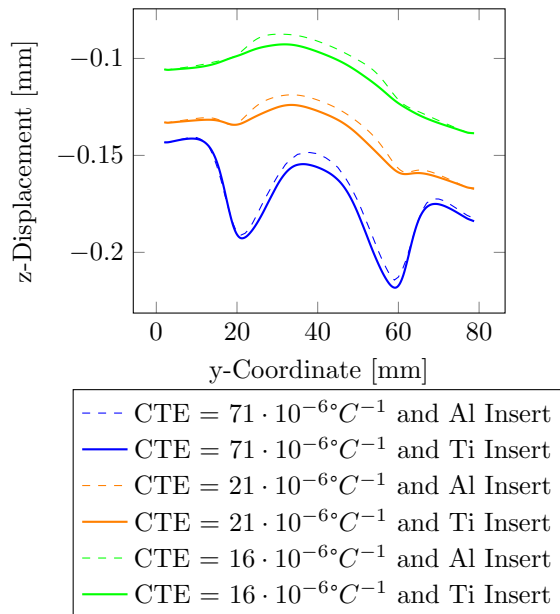

Figure 18: Solar Cell Thermal Deformation (Cold Case)

Titanium was selected for the blind insert material whereas the potting material selected was a low-CTE epoxy. For the hot case, M_c was 48% while, for the cold case, M_c was 15%. This material combination is the only one that led to positive margins for both temperature extremes.

TESTING

A series of tests were performed to qualify the HDRM design. Thermal cycling, thermal chamber deployments, and vibration tests were completed. The wing was undergoing thermal vacuum chamber (TVAC) testing at the time of writing this paper which would validate the deployment under the combined effect of temperature and vacuum. It is noteworthy to mention that multiple deployments of the wing were performed. The seamless stowing and deployment of the wing also enabled the validation of the cup-cone jamming analysis.

Thermal Test

Many aspects of the wing were to be verified via thermal testing. Specifically for the HDRM, the HDRM bolt spring mechanism, and the strength of solar cells mounted above the blind inserts needed to be validated.

Hot and cold deployment tests were performed in a thermal chamber where the selected temperatures were set based on the operating temperature limits of the ERM. Due to volumetric limitations, the full wing could not be deployed inside the thermal chamber. Consequently, a short mass simulator was used which was designed to match the moment of inertia of the wing about the hinge axis (Figure 19).
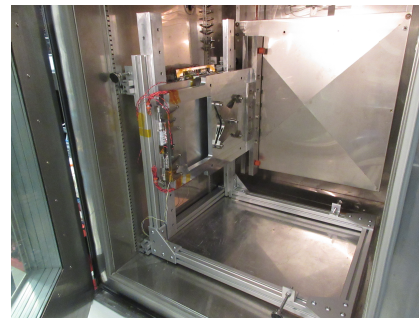

Figure 19: Thermal Chamber Test Setup

The mass simulator could be configured to match either the moment of inertia of the fully deployed wing or that of the wing where the outer panel remains in contact with the inner panel for the full 90° rotation of the hinge attached to the bus. The latter reproduces the scenario where the outer panel rotates significantly slower than the inner one. This is the critical case presented earlier where the ERM coupler could lock itself with the ERM stem. This was the reason behind the integration of a spring pushing off the HDRM bolt. Therefore, such test setup enabled the testing of the spring mechanism. Moreover, wire harnesses were added as they rep-

resented a source of resistance torque to the spring-loaded hinges. Even though only one panel was used, the HDRM bracket was mounted in the same location relative to the other components as if both panels were present by use of spacers. With the use of the spring housed within the HDRM bracket, both hot and cold deployments were successful, proving the efficacy of the spring design.

Solar cells were applied on the Qualification Model (QM) solar panel on the opposite face to the blind inserts used for the HDRM bracket. As mentioned earlier, this was the critical location for solar cell cracking due to CTE mismatch. The QM solar panel was subjected to 100 thermal cycles varying from -70°C to +110°C. Although the components were design to go down to -100°C, the minimum temperature that could be reached was -70°C due to testing facility limitations.

To verify the state of the solar cells, a glow test was performed before and after the thermal cycling test. A glow test consists of supplying current to the solar cell string in a dark room allowing it to illuminate and show damage such as cracks that may have occurred post-environmental testing (Figure 20).
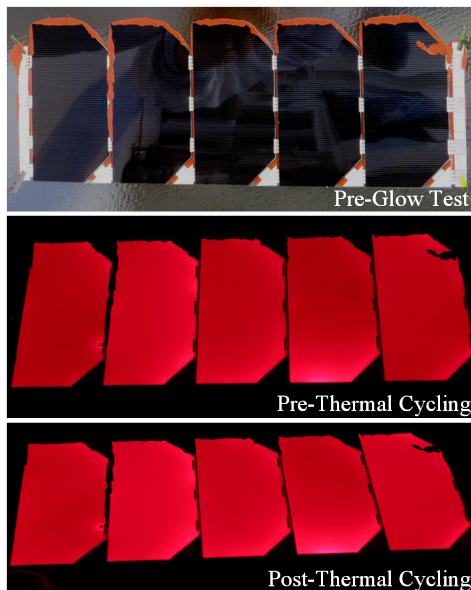

Figure 20: Pre and Post-Thermal Cycling Glow Test

As demonstrated by the before and after pictures of the glow test, no damage was sustained from the thermal cycling which verifies the outcomes of the thermal strain analysis (Figure 20). Note that the black area at the top right corner is only silicone which flowed over the edges. This does not impact any of the results of the qualification tests.

Vibration Test

A series of vibration tests were performed with the QM wing mounted to the QM satellite. The tests included qualification level sine burst tests ($>14G$), random vibration tests ($>8G_{RMS}$), sine tests, and low-level sine sweeps. The test profiles were composite profiles based on requirements from a list of potential launch providers such as to maximize mission opportunities.

The wing remained stowed for the entirety of the tests with negligible shift in its first few stowed natural frequencies ($<5\%$ shift), proving that the HDRM components were sized properly. The wing was successfully deployed after the tests (Figure 21). The first natural frequency of the deployed wing decreased by $<3\%$.
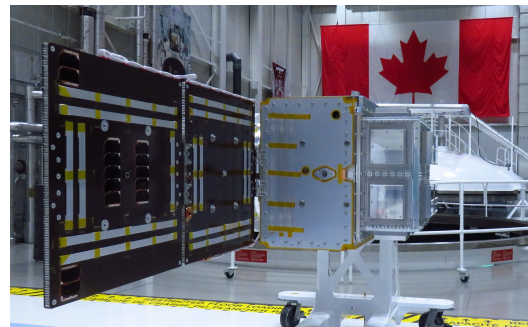

Figure 21: Post-Vibration Test Deployment

Examinations of the cups and cones after vibration testing showed no yielding and minimal wear on the contact surfaces (Figure 22). A sample cone was further cleaned with isopropyl alcohol to better observe the wear. Most of the coating remained undamaged. The completion of TVAC tests will confirm that the wear does not impact the deployment.
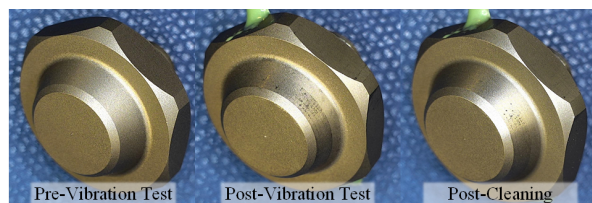

Figure 22: Contact Interface Wear

Finally, a glow test was performed again and showed no signs of damage on the solar cells (Figure 23).
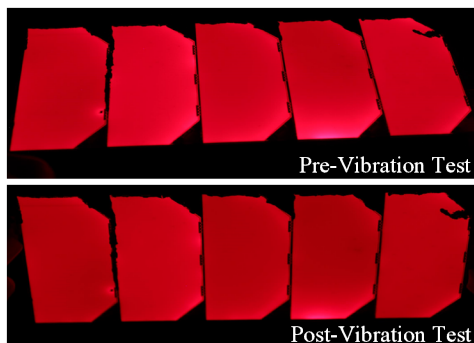
Figure 23: Pre and Post-Vibration Glow Test

CONCLUSION

The increasing use of deployable structures such as solar wings is inevitable to push the boundaries of small satellite missions. However, they add risk, complexity, and costs.

SFL required an in-house solution for deployable solar wings of its small satellite platform. For the solution to be low-cost and reliable, a simple and robust HDRM was designed. Its main components are the ERM to release the wing once in orbit, the cup and cones to support the majority of the shear loads, and the HDRM bracket to transfer the preload from the HDRM bolt to the cups and cones.

Quasi-static and dynamic analyses were performed to determine the preload required to avoid cup and cone separation. The half-angle on the cup-cone interface was selected based on minimizing the preload required, and avoiding interference and self-holding tapers. The size of the interface was determined based on a contact analysis where the material strength margins were found to be above 26%. The HDRM bracket was designed in the shape of an arch to reduce the shear loads on the inserts. This led to insert strength margins of 26%. A thermal strain analysis showed that the thermal deformations would not damage the solar cells. There was 48% of margin on the curvature for the hot case and 15% for the cold case.

Thermal tests showed successful deployments at temperature extremes and no damage to the solar cells. The wing was subjected to a series of vibration tests and successfully deployed afterwards. In comparison to the pre-vibration test data, the first few natural frequencies of the stowed wing decreased by <5% and the deployed wing first natural frequency decreased by <3%. Negligible wear was present on the cup-cone interfaces and no damage was observed on the solar cells. The QM wing was undergoing thermal vacuum testing at the time of writing this paper.

References

[1] A. River and A. Stewart. Study of spacecraft deployables failures. In *Proceedings of the 19th European Space Mechanisms and Tribology Symposium*, 2021.

[2] J.-F. Castet and J. H. Saleh. Satellite and satellite subsystems reliability: Statistical data analysis and modeling. *Reliability Engineering and System Safety*, pages 1718–1728, 2009.

[3] European Cooperation for Space Standardization. *ECSS-E-ST-32-10C - Space Engineering, Structural Factors of Safety for Spaceflight Hardware*, 2009.

[4] J. Abdo and M. Tahat. The effect of frequency and amplitude of vibration on the coefficient of friction for metals. *WSEAS Transactions on Applied and Theoretical Mechanics*, pages 265–274, 2008.

[5] National Aeronautics and Space Administration. *NASA-STD-5020A - Requirements for Threaded Fastening Systems in Spaceflight Hardware*, 2018.

[6] D. Bozkaya and S. Müftü. Mechanics of the tapered interference fit in dental implants. *Journal of Biomechanics*, 2002.

[7] M. T. Dugger and D. A. Chinn. Surface roughness of anaodized coatings. *Sandia National Laboratories*, 2010.

[8] European Cooperation for Space Standardization. *ECSS-E-HB-32-22A - Space Engineering, Insert Design Handbook*, 2011.